Blockage influence on bi-stable flows of a notchback bluff body

(article starts on next page)

Blockage influence on bi-stable flows of a notchback bluff body

Kan He (何侃),[1,2,3,4] (iD) Guglielmo Minelli,[5] Xinchao Su (苏新超),[4] (iD) Guangjun Gao (高广军),[1,2,3,a] and Siniša Krajnović[4] (iD)

AFFILIATIONS

[1]Key Laboratory of Traffic Safety on the Track of Ministry of Education, School of Traffic & Transportation Engineering, Central South University, Changsha 410075, China
[2]Joint International Research Laboratory of Key Technology for Rail Traffic Safety, Central South University, Changsha 410075, China
[3]National & Local Joint Engineering Research Center of Safety Technology for Rail Vehicle, Changsha 410075, China
[4]Division of Fluid Dynamics, Department of Mechanics and Maritime Sciences, Chalmers University of Technology, SE-41296 Gothenburg, Sweden
[5]Aerodynamics, Volvo Cars, SE-41878 Gothenburg, Sweden

[a]Author to whom correspondence should be addressed: gjgao@csu.edu.cn

ABSTRACT

The expected flow asymmetry behind a three-dimensional notchback Ahmed body is numerically investigated using large-eddy simulations with different blockage ratios of 0%, 5%, 10%, and 20%. The focus of the study is on the natural bi-stable flow influenced by the blockage ratio. Although the wake asymmetry can be observed under the blockage ratio within $0\% - 10\%$, the significant blockage influence on the sensitive bi-stability is indicated by the wake structures, pressure gradients, and wake dynamics achieved with the proper orthogonal decomposition. The higher blockage ratio increases the turbulence kinetic energy, velocity, and negative pressure in the near-wake region, resulting in the decrease in the asymmetry degree. The consistency of the asymmetric wake is found with blockage ratios between 0% and 5%. However, a 20% blockage ratio symmetrizes the bi-stable wake. Several existing drag corrections for the blockage influence are discussed. The wind tunnel experiment verifies the bi-stable flow with low blockage ratios and the wake symmetrization with a 20% blockage ratio.

Published under an exclusive license by AIP Publishing. https://doi.org/10.1063/5.0077251

I. INTRODUCTION

The aerodynamic drag and stability of road vehicles are dependent on their surrounding flow topology. The experimental exploration of flows for full-scale cars in open-air conditions is usually difficult to carry out with a high level of accuracy. Therefore, the exploration of the flow characteristics is widely based on the analysis of the scaled models taking advantage of the wind tunnel experiments. Benefited from this method, the boundary conditions are more accurately controlled, enabling detailed analysis of the vehicle's geometry on the resulting flow. However, for the wind tunnel experiment, the model placed in a limited section with boundaries results in a distortion of reality. For this reason, the accuracy of the tested flow is ascribed to the quantification of the blockage ratio effect.

The blockage ratio leading to the acceleration of the flow deviates the pressure, aerodynamic forces, and wakes of the tested model. As observed by Maskell (1963), the blockage influence needs to be taken into account for wake separations of the bluff body. Particularly, Takeda and Kato (1992) suggested that the models forming the flow reattachment were found more sensitive to the blockage ratio. Therefore, the ground vehicle with the slanted rear possibly leading to the reattachment in the wake requires the consideration of the blockage influence on the surrounding flow. An example is the notchback car representing the sedan with a slanted window and a trunk in the rear part of the body, allowing the reattachment on the trunk (Carr, 1974). Subsequently, numerous studies for the notchback cars have demonstrated the accuracy of the resulted surrounding flow depending on the blockage influence. For example, comparative force measurements on full-scale notchback vehicles performed between several wind tunnels were investigated by Buchheim et al. (1980); Cogotti et al. (1980); and Carr (1982). The aerodynamic drag increased by the higher blockage was found by Carr and Stapleford (1986), who proposed an efficient drag correction with the blockage ratio within the range of $3.5\% - 10\%$. Moreover, the blockage influence on passenger cars under yaws was investigated by Mercker (1986). According to the experimental data given in Wickern (2001), it can be found that the blockage ratio under 5% results in a lower increasing rate of the drag.

In addition, the exploration of the blockage effect on vehicles can benefit from numerical simulations. The blockage influence on a sedan, a sport utility vehicle, and a pickup truck was studied by Yang *et al.* (2005) using the numerical method. In addition, the flow around a notchback car, under conditions of the free air, the slotted wall, the adaptive wall, and the open jet, was numerically investigated by Connor *et al.* (2006). More recently, Altinisik *et al.* (2015) has proved the influence of the blockage ratio on the notchback car showing the consistency of the results under the blockage ratio of 5%.

Summing up the literature, it can be concluded that the distortion on account of the low blockage ratio (under 5%) seems acceptable and more easily corrected. On the other hand, the high blockage ratio triggering the acceleration of the flow influences the pressure distribution, culminating in the inaccuracy of the measurement. Moreover, the interference of the boundary walls is more significant under the high blockage condition, leading to difficulties in the definition of blockage corrections. Although the distortion caused by the blockage ratio has been corrected for extensive applications (Stafford, 1981; Hackett and Cooper, 2001; Cooper *et al.*, 2008), previous investigations focusing on the blockage effects assumed the symmetric flow of the axisymmetric models. However, for the notchback car, the symmetry breaking of the wake has been observed by Cogotti (1986), suggesting a small yawing angle triggering the wake switch between two states. Since then, the asymmetry of the flow being sensitive to the perturbation of the free-stream velocity has been confirmed by Lawson *et al.* (2007). A more recent experimental study investigated by Yan *et al.* (2019) presented the asymmetry of the wake behind a notchback car model. Furthermore, the wake asymmetry was found for the simplified notchback Ahmed body (Sims-Williams *et al.*, 2011). This geometry originates from the hatchback Ahmed body (Ahmed *et al.*, 1984) by adding a trunk attached to the rear vertical base. The wake bi-stability of the notchback Ahmed body has been previously confirmed in large-eddy simulation (LES) by He *et al.* (2021b).

Not only the notchback vehicle but also the squareback Ahmed body has been found to form the wake asymmetry (Grandemange *et al.*, 2012). The wake bi-stability characterized by random switches between two asymmetric counter states was proposed by Grandemange *et al.* (2013). In addition, the bi-stable flow of a squareback Windsor body was reported by Pavia *et al.* (2018; 2020). The bi-stable wake can be classified as a special case of the flow multi-modality for axisymmetric geometries, like the sphere (Grandemange *et al.*, 2014) and the bullet-shaped cylinder (Rigas *et al.*, 2014; Pavia *et al.*, 2019). The multi-stable wake shows the asymmetry in temporal periods. However, the statistic flow is symmetric on the account of

frequent switches of the wake between the infinite numbers of azimuthal symmetry planes.

For the wake bi-stability behind the squareback Ahmed body, the literature has proved the sensitivity to small perturbations of the wake (Cadot *et al.*, 2015; Evrard *et al.*, 2016; Barros *et al.*, 2017; Bonnavion and Cadot, 2018). Therefore, the acceleration of surrounding flows as a result of a higher blockage ratio may change the wake structures, affecting the bi-stable wake state. For this reason, the present work aims to inquire about the blockage influence on the wake bi-stability. Considering the wake behind the notchback configuration involving the interaction of separations and reattachment, the wake asymmetry formed behind the notchback Ahmed body (Sims-Williams *et al.*, 2011) is selected as the studied flow. Performing LES to predict the bi-stable wake behind the squareback (Östh *et al.*, 2014; Evstafyeva *et al.*, 2017; Lucas *et al.*, 2017; Dalla Longa *et al.*, 2019) and the notchback (He *et al.*, 2021a; 2021b; 2021c). Ahmed bodies has proved to be successful due to its possibility to resolve the highly turbulent flow. Thence, the present work is also based on the numerical simulation applying the LES method. The mechanism of the significant blockage influence on the wake asymmetry is explored by analysis of the near-wall flow. The results of the present paper are intended to serve as the baseline for future investigations concerning the wake bi-stability behind bluff bodies.

The remainder of the paper is organized as follows. Section II presents the description of the methodology. Results of the blockage effect on the wake bi-stability are discussed in Sec. III. Conclusions follow in Sec. IV. The description of the mesh resolution is presented in Appendix A. Validation of the blockage effect is given in Appendix B. Equations for blockage corrections are presented in Appendix C.

II. METHODOLOGY
A. Description of geometries and boundary conditions

The geometry used for numerical simulations is a notchback Ahmed body. The wake behind this model is expected to be asymmetric following the previous experimental observation (Sims-Williams *et al.*, 2011). The dimensions of the body shown in Fig. 1 are expressed in the model height, $H = 0.096$ m. The model width is $W = 1.35H$, the model length is $L = 3.82H$, the deck length is $L_D = 0.469H$, and the deck height is $H_D = 0.687H$. The clearance between the ground and the bottom body is $H_C = 0.21H$. The effective backlight angle is $\beta = 17.8°$, giving roof length $L_S = 2.847H$. The reference axis is linked to the model. The origin of the coordinates is located at the central model length in the x-direction, the central model width in the y-direction, and the bottom model in the z-direction.
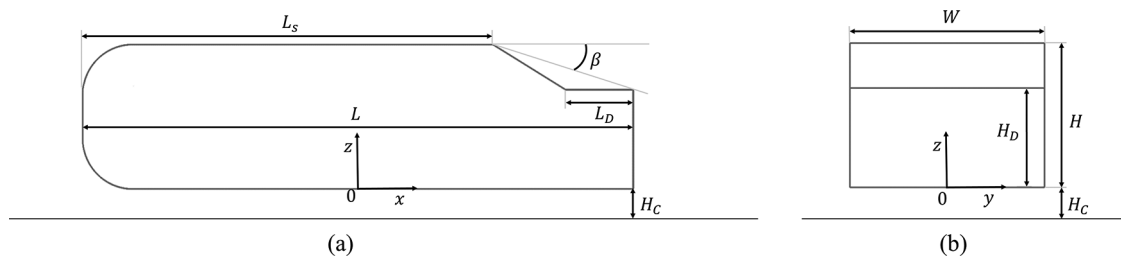

FIG. 1. Geometric model: (a) side view; (b) back view.

Four digital tunnels giving blockage ratios of 0 (blockage-free), 5%, 10%, and 20%, denoted as BR0, BR5, BR10, and BR20, respectively, are illustrated in Fig. 2(a). The change of the blockage ratio is achieved by varying the width (W_T) and the height (H_T) of the tunnel with a constant $W_T/H_T = 2$. An example presented in Fig. 2(b) shows the side view of BR5. The inlet is set at $8H$ upstream of the model, and the outlet is located at $19H$ downstream of the model. For all cases, the Reynolds number, $Re = 5 \times 10^4$, is based on the model height and the uniform free-stream velocity, $U_{inf} = 7.864$ m/s. The pressure outlet with a constant of 0 Pa is set at the downstream boundary. The no-slip wall boundary condition is used on the ground and the surface of the model. In BR0, the lateral surfaces and the roof of the tunnel are set as symmetry planes, to virtually expand the domain matching the blockage-free condition. However, those for BR5, BR10, and BR20 are treated as no-slip walls, following the testing section of the wind tunnel.

B. Numerical methods

The governing LES equations, solved with a commercial finite volume solver, Star CCM+ 2019.2, are the incompressible Navier–Stokes and the continuity equations filtered with the implicit spatial filter of characteristic width Δ. The filter width, Δ, is defined as $\Delta = (\Delta_1 \Delta_2 \Delta_3)^{1/3}$, where Δ_i are the computational cell sizes in three coordinate directions. The wall-adapting local eddy-viscosity (WALE) model proposed by Nicoud and Ducros (1999), which has been successfully applied to predict wakes of the hatchback Ahmed body (Krajnović and Davidson, 2005; Aljure et al., 2014), and symmetry-breaking modes behind the notchback Ahmed body (He et al., 2021b; 2021c), is used in this work. This SGS model is based on the square of the velocity gradient tensor and accounts for the effects of the strain and rotation rates. The sub-grid eddy viscosity in the WALE model is modeled as

$$\mu_t = \rho (C_w \Delta)^2 \frac{\left(S_{ij}^d S_{ij}^d \right)^{3/2}}{\left(\tilde{S}_{ij} \tilde{S}_{ij} \right)^{5/2} + \left(S_{ij}^d S_{ij}^d \right)^{5/4}}, \tag{1}$$

11.46H

7.36H

5.2H

3.62H

BR0
BR5
BR10
BR20

5.73H

3.68H

2.6H
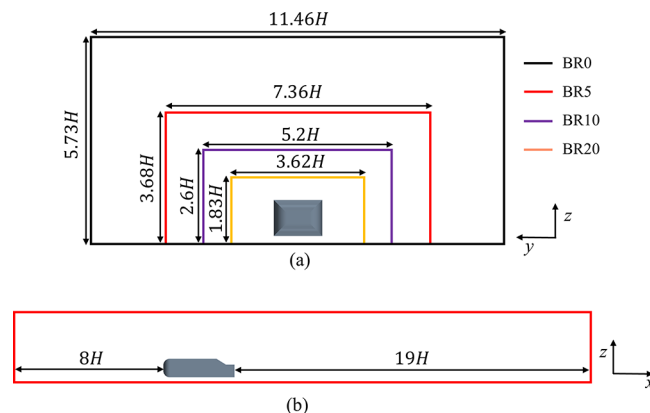
1.83H

(a)

8H   19H

(b)

FIG. 2. The flow domains: (a) front view of cases with different blockage ratios; (b) side view of BR5.

where the C_w is a constant, here $C_w = 0.544$. $\tilde{S}$ is the filtered rate of strain tensor, and S_{ij}^d is the traceless symmetric part of the square of the velocity gradient tensor g_{ij}, defined as

$$S_{ij}^d = \frac{1}{2} \left(\tilde{g}_{ij}^2 + \tilde{g}_{ji}^2 \right) - \frac{1}{3} \delta_{ij} \tilde{g}_{kk}^2, \tag{2}$$

where g_{ij} denotes $\partial u_i / \partial x_j$.

Convective fluxes are approximated by a blend of 98% central difference scheme and 2% upwind scheme. The time integration is done using the second-order accurate three-level time Euler scheme. The non-dimensional time step $dt^* = \Delta t_s U_{inf}/H = 3.44 \times 10^{-3}$, giving a Courant-Friedrichs-Lewy (CFL) number lower than 1 in over 99% of the cells during all time steps. The Reynolds-averaged Navier-Stokes (RANS) equations are applied obtain the initial condition. Then, the LES approach is performed for $t^* = tU_{inf}/H = 186$ corresponding to six flow-through passages through the tunnel. The sampling duration of each simulation is $t^* = 124$ after an initial period of $t^* = 62$ for the physical establishment of the flow. The mesh resolutions and the grid independence examination are presented in Appendix A. The validation of the simulation is presented in Appendix B.

C. Measurements of the aerodynamic force, velocity, and pressure

The aerodynamic drag force F_d is the components of the aerodynamic load in the x-direction associated with the coordinate system defined in Fig. 1. The associated aerodynamic drag, C_d, is defined as

$$C_d = \frac{F_d}{\frac{1}{2} \rho A U_{inf}^2}, \tag{3}$$

where ρ is the density of the fluid, A is the projected area of the frontal model surface, and U_{inf} is the free-stream velocity.

The velocity components in the x, y, and z directions are U_x, U_y, and U_z, respectively. The associated streamwise and spanwise velocity components, u, v, and w, are defined as

$$u = \frac{U_x}{U_{inf}}, \quad v = \frac{U_y}{U_{inf}}, \quad w = \frac{U_z}{U_{inf}}. \tag{4}$$

The coefficient of pressure C_p is defined as

$$C_p = \frac{p - p_\infty}{\frac{1}{2} \rho U_{inf}^2}, \tag{5}$$

where p is the pressure and p_∞ is the pressure in the upstream far field used as the reference.

D. Description of the modal analysis

The proper orthogonal decomposition (POD) is used to perform modal analysis of the wake flow for an in-depth understanding of flow structures in terms of both energy contents and characteristic frequencies. As originally proposed by Lumley (1970), and later introduced with the method of snapshots by Sirovich (1987), this method is based on the energy ranking of orthogonal structures predicted from a correlation matrix of the snapshots. A singular value decomposition (SVD) approach is used to conduct the POD analysis. The time step between

snapshots is $\Delta t = 4.2 \times 10^{-4}$s, 10 times the Δt_s in simulations, giving the considered highest frequency (the Nyquist frequency) of 1190 Hz. The lowest frequency is limited by the snapshot total sampling time to 7 Hz (the snapshots are collected more than $t^* = 124$, and at least ten periods should be captured for a reliable frequency evaluation). Therefore, the reliable real frequency is between 13 and 1190 Hz ($0.16 < S_{tH} < 14.52$). The non-dimensional frequency St_H is the Strouhal number normalized with the free-stream velocity and the height of the model.

III. ANALYSIS AND DISCUSSION

This section presents the results predicted with cases of BR0, BR5, BR10, and BR20. The increase in the blockage ratio directly acts on the flow acceleration around the body, resulting in the change of pressure. Shown in Figs. 3(a)–3(d) are the pressure distribution projected on the central Y_0 plane. For all cases, the pressure in front of the forebody is positive due to the flow impingement. The negative pressure can be observed around the rounded surfaces and in the wake concerning the local flow separations. For quantitative analysis, the pressure profiles on the surface curve, S_0, representing the central line of the top-half body, are presented in Fig. 3(e). It can be seen that the pressure distributions between BR0 and BR5 are in good agreement. The BR10 case shows a decrease in global pressure. With a further increase in the blockage, a distinct lower pressure is observed with BR20. Given that the wake is supposed to be asymmetric, the difference in the pressure distribution around the body is expected to influence the flow structures responsible for the extent of wake asymmetry.

The remaining part of this section proceeds as follows. Section III A presents the flow states under the influence of the blockage ratio. In Sec. III B, the underlying mechanism of the blockage influence on the degree of wake asymmetry is explored from the perspective of near-wall flow structures and wake dynamics. Section III C discusses the aerodynamic drag influenced by the blockage ratio.

A. Flow states

The flow structures identified by mean iso-surfaces of the Q-criterion are presented in Fig. 4. Here, the non-dimensional Q^* is normalized with the free-stream velocity, U_{inf}, and the model height, H, given by

$$Q^* = QH^2/U_{inf}^2. \tag{6}$$

In Fig. 4, the vortex V_c shedding from the near-wall region of the roof's trailing edge, and two C-pillar vortices, V_l and V_r, are recognized. Particularly, the wake asymmetry is indicated in BR0–10. For BR0 and BR5, V_c deflects to the left side to interact with V_l, showing the S_B state. Thus, V_l is disturbed but V_r on the right side can extend further downstream. For BR10, V_c deflects to the right side, showing the opposite asymmetry in the S_A state. The S_A and S_B are the mirrored asymmetric states that randomly appear in the simulation, showing the bi-stability. However, for BR20, the wake symmetry is indicated, showing V_c in the center with no deflections. Thus, the flow is in the symmetric S_C state. For clarity of comparisons, the numerical results of the asymmetric cases are presented in the same normalized state by mirroring S_A to S_B.

Although the flow averaged throughout the sampling duration for $t^* = 124$ includes over 3.6×10^4 time steps, the physical time $t = t^* H/U_{inf} = 1.52$ s is much lower than the timescale of the asymmetric state that can last for tens of seconds (see Appendix B). For this reason, the random switch of the bi-stable wake is not captured in the present work due to the limitation of the physical time. However, the readers can refer to He et al. (2021b) for details of the wake switching process and the mirrored asymmetric states of the studied flow.

The distribution of the mean streamlines and the spanwise vorticity, $\overline{\Omega_y}$, projected on the section planes, Y_1 and Y_2, are presented in Fig. 5. The vorticity is normalized with the free-stream velocity, U_{inf}, and the model height, H. For all cases, the wake separation can be
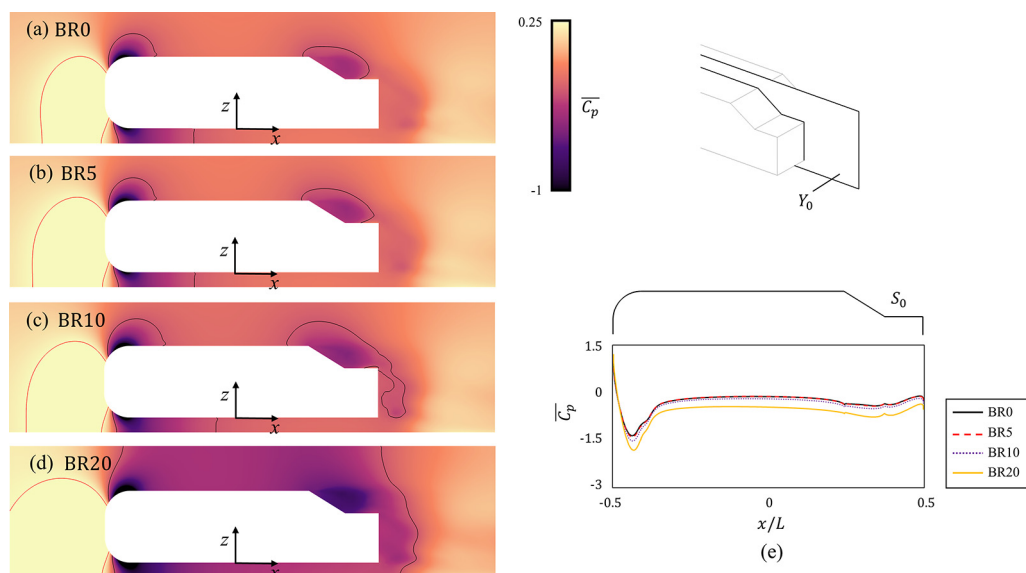

FIG. 3. Distribution of the mean pressure, $\overline{C_p}$, on the central Y_0 plane, with contour lines of $\overline{C_p} = -0.25$ (shown black) and $\overline{C_p} = 0.25$ (shown red). (a) BR0; (b) BR5; (c) BR10; (d) BR20. (e) Profiles of $\overline{C_p}$ on the central line of the body surface, S_0.
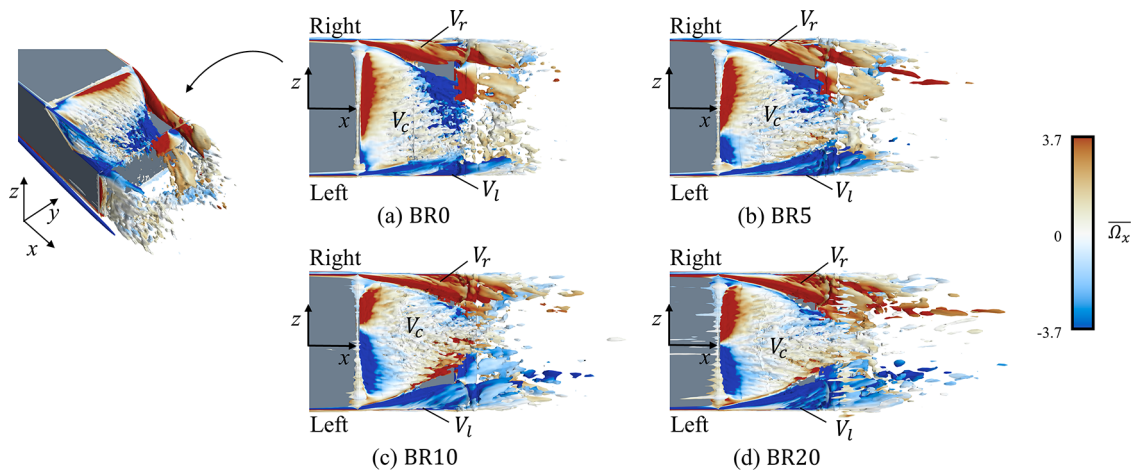
FIG. 4. Flow structures behind the slant, visualized by the time-averaged iso-surface of the second invariant of the velocity at $Q^* = 3.7$: (a) BR0; (b) BR5; (c) BR10; (d) BR20.

identified by $\overline{\Omega_y}$, showing the vortex V_c separating from the shear layer of the roof, V_b from the deck's trailing edge, and V_g from the bottom body. In addition, on the Y_2 plane, the flow reattaching to the deck is indicated in the streamlines. However, the flow on the Y_1 plane separating from the upper slant extends further, moving over the deck. The quantitative assessment of the wake asymmetry can be indicated in the length of V_c, denoted L_{VC}, and the deck reattachment length, L_R. Here, L_{VC} is defined as the distance between the roof and the local maximum x-coordinate on the contour line of $\overline{\Omega_y} = 3.7$. L_R is defined as the distance between the positive-negative transition point of near-wall $\overline{\Omega_y}$ and the deck's trailing edge. Therefore, comparing L_{VC} and L_R on the two planes, the asymmetry is presented in BR0–10. However, the symmetry in BR20 is indicated in the equivalent separations and reattachments on the two sides.

The asymmetric flow reattachment on the deck leads to the pressure difference on two sides. Therefore, the time history of the flow state can be identified by the pressure gradient on the deck. To obtain the pressure signals, two monitoring points, P_{dl} and P_{dr}, are set on two sides of the deck shown in Fig. 6. The distance between the central line and each point is $dy = 0.417H$. The points are at $D_{P2} = 0.5L_D$ (half-length of the deck) from the deck's trailing edge. With the pressure signals, the degree of the asymmetric can be quantified by the deck pressure gradient, defined as

$$\frac{\partial C_{pd}}{\partial y} = \frac{C_p(P_{dr}) - C_p(P_{dl})}{2dy/H}, \tag{7}$$

where $C_p()$ represents the sampled pressure coefficient on each monitoring point. By the definition, the high absolute value of $\partial C_{pd}/\partial y$ indicates the high degree of wake asymmetry. On the other hand, $\partial C_{pd}/\partial y$ around 0 suggests the wake symmetry.

The time history of $\partial C_{pd}/\partial y$ obtained from the four simulations is presented in Fig. 7. For BR0-10, $\partial C_{pd}/\partial y$ fluctuates with positive values. Thus, it can be deduced that during the sampling period the wake is always in one of the asymmetric states without switches to the opposite side. For BR20, $\partial C_{pd}/\partial y$ fluctuates around 0, showing symmetry. The quantitative comparison of $\partial C_{pd}/\partial y$ between the four

cases is achieved by the power density function (PDF) shown in Fig. 7(e). For cases BR0-10, although the asymmetry is indicated in the positive peaks of PDF, the lower peak value with the higher blockage shows the decrease in the asymmetry. However, for BR20, the asymmetry is indicated by the PDF of $\partial C_{pd}/\partial y$ concentrating around 0. Particulary, it can be seen that $\partial C_{pd}/\partial y$ fluctuates between negative and positive values during the simulation period, showing high-frequency switches. In terms of the mean values, $\overline{\partial C_{pd}/\partial y}$ averaged throughout the sampling duration gives 0.649, 0.618, 0.53, and 0.043, respectively, for BR0, BR5, BR10, and BR20. Therefore, although the wake asymmetry can be predicted with BR0–10, the degree of the asymmetry remains to decrease with the higher blockage ratio. Compared to BR0, the deviation of 4.89% for BR5 and 20.19% for BR10 are evaluated by $\overline{\partial C_{pd}/\partial y}$. Considering the accuracy of the asymmetry, a blockage ratio of at least 5% is required for the bi-stable wake.

B. Flow mechanisms

Understanding the wake state influenced by the blockage ratio requires a deeper analysis focusing on the notchback region since the downstream flow is attributed to the separation behind the rear slant. The in-depth exploration of the wake dynamics behind the slant is investigated by the modal analysis applying POD to the pressure snapshots projected on the Z_1 plane behind the slant. The POD modes are identified by the energy content. The first six modes sorted by the ranking of the energy content are presented in Fig. 8, where mode 1 corresponds to the averaged field containing most of the energy. The subsequent modes distributed in pairs show the gradual decrease in the energy content.

The flow structures projected on the horizontal Z_1 plane behind the slant are presented in Fig. 9. The distribution of the mean streamwise velocity, $\overline{u}$, is shown in Figs. 9(a)–9(d). From this visualization, the deflection of V_c is presented in BR0–10. However, for BR20, V_c remains in the center showing symmetry. Furthermore, the wake dynamics is identified by POD in the Z_1 plane. The wave packets
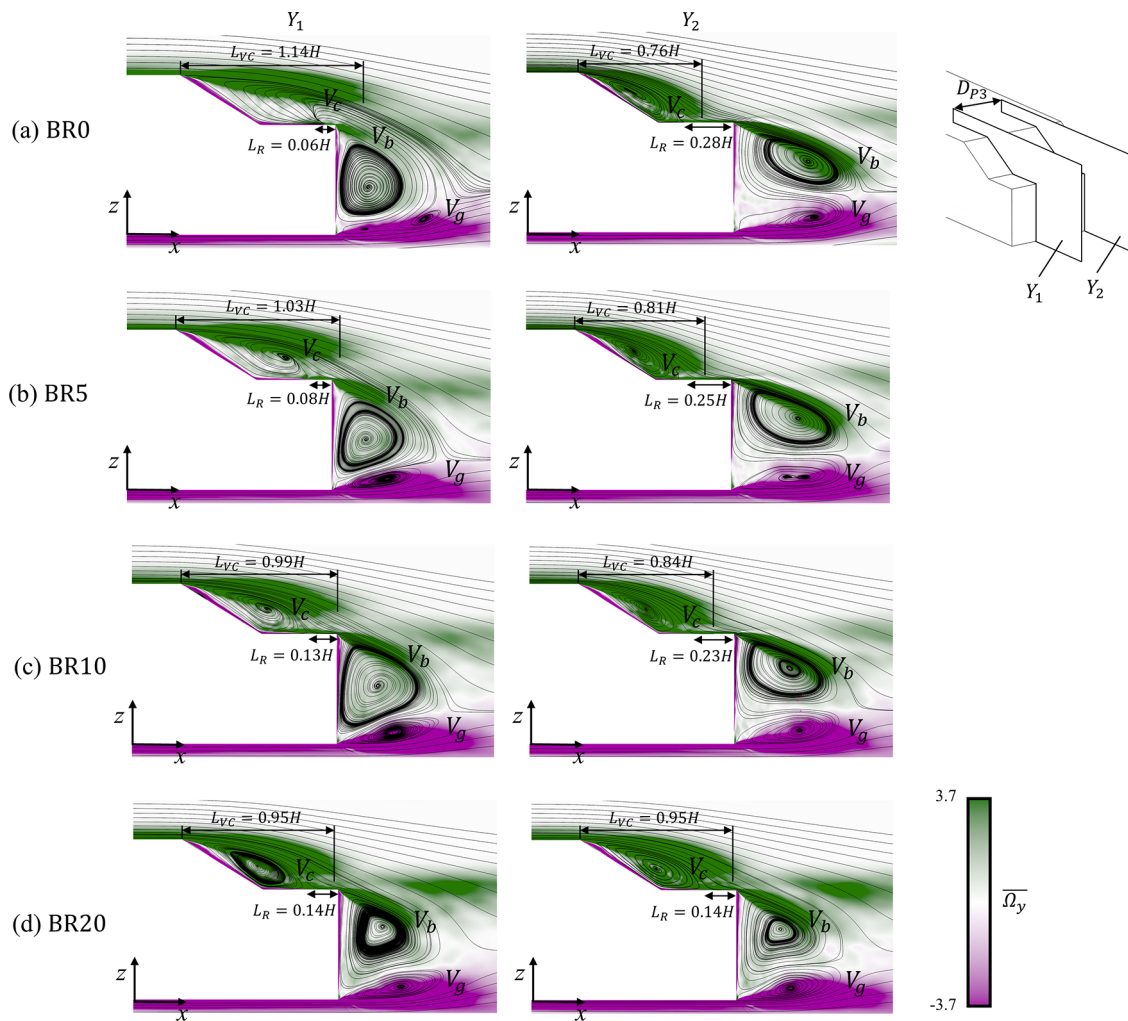
FIG. 5. Mean streamlines and spanwise vorticity $\overline{\Omega_y}$ on the Y_1 and the Y_2 planes. The distance between Y_1 and Y_2 is $D_{P3} = 0.5W$ (half-width of the model): (a) BR0; (b) BR5; (c) BR10; (d) BR20.
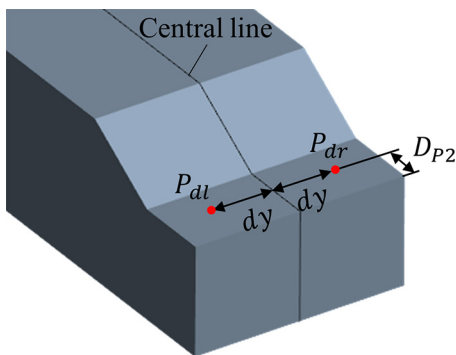

FIG. 6. Pressure monitoring points on the deck.

presented in Figs. 9(e)–9(h) are recognized by Mode 2 ranking the second energy content. The cases of BR0-10 are in agreement, indicating V_c moving downstream on the left side, following the left deflection of V_c shown in Figs. 9(a)–9(c). The difference is found in BR20, showing that V_c moves downstream in the center, in accordance with Fig. 9(d). Moreover, the associated power spectral density (PSD) of mode 2 presented in Figs. 8(i)–8(l) confirms the identical main frequency between BR0 and BR5. For BR10, the main frequency becomes slightly higher and further increases with the blockage ratio reaching BR20.

To seek the near-wall separation determining the status of V_c, the flow structures projected on the Z_0 plane behind the upper slant, visualized by the distribution of the mean streamwise vorticity, $\overline{\Omega_x}$, are presented in Figs. 10(a)–10(d). It can be seen that V_c separating from the roof's trailing edge consists of two sub-structures, V_{cl} and V_{cr}, respectively, on the left and right sides of the shear-layer region.
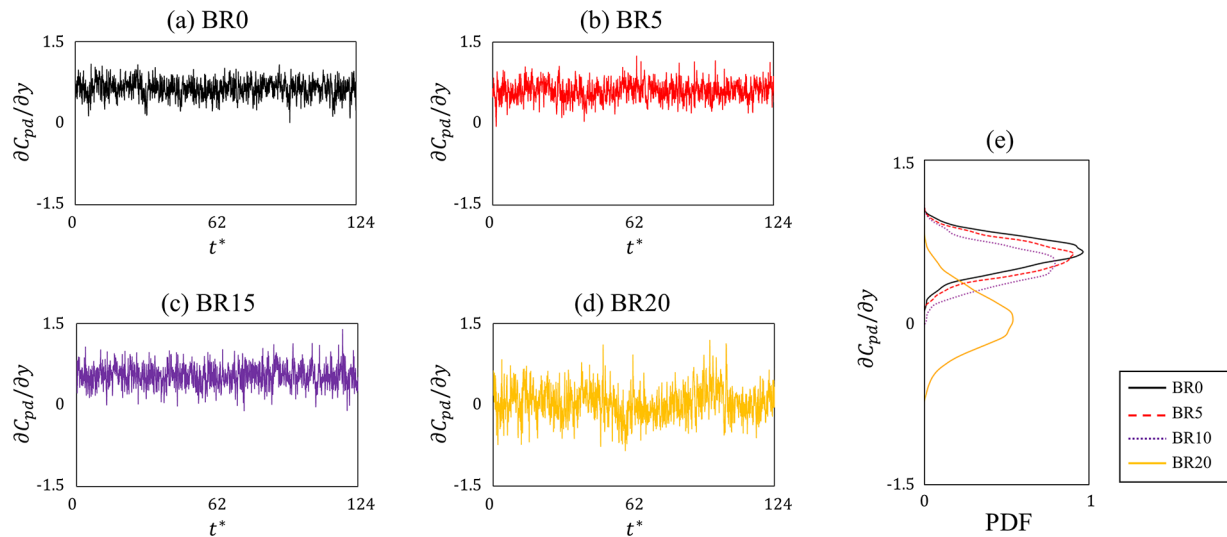
FIG. 7. The time history of the deck pressure gradient, $\partial C_{pd}/\partial y$: (a) BR0; (b) BR5; (c) BR10; (d) BR20; (e) PDF of $\partial C_{pd}/\partial y$.

For the three asymmetric wakes with BR0-10, V_{cr} is dominant, showing a larger separation region attached to the upper slant. However, for BR20, V_{cl} and V_{cr} are equivalent, showing symmetry.

The dynamics of these shear-layer vortices can be characterized by mode 3 of POD projected on the Z_1 plane, as shown in Figs. 10(e)–10(h). For BR0-10, mode 3 describes the direction of V_{cr}, indicating the deflection to the left side. Since the dynamics of the opposite V_{cl} is invisible in the first four POD modes, it can be speculated that V_{cr} is more energetic than V_{cl}. Therefore, the global status of V_c governed by the dynamics of V_{cr} shows the deflection to the left side, indicating the asymmetry. On the other hand, for BR20, since V_{cl} and V_{cr} are comparable, mode 3 indicates their direction moving downstream without deflections. Thus, V_c considering the synthetic direction of V_{cl} and V_{cr} moves downstream in the center. In addition, Figs. 10(i)–10(l) show the associated PSD of mode 3. The main frequency in BR0 and BR5 shows good agreement. However, with the higher blockage ratio, the main frequency decreases.

The underlying mechanism responsible for the status of the near-wall vortices around the roof's trailing edge is explored by the turbulence kinetic energy (TKE). Here, TKE is defined as

FIG. 8. The energy content of the top six modes for the POD analysis applied to pressure snapshots projected on the Z_1 plane.

$$\text{TKE} = \frac{1}{2}\left[\overline{(u')}^2 + \overline{(v')}^2 + \overline{(w')}^2\right], \quad (8)$$

where $\overline{(u')}^2$, $\overline{(v')}^2$, and $\overline{(w')}^2$ are the mean Reynolds stress components in the streamwise, the spanwise, and the vertical directions, normalized by U_{inf}^2.

The distribution of TKE projected on the X_1 plane is presented in Figs. 11(a)–11(d). Focusing on the near-wall region above the roof, it is found that the TKE increases with the higher blockage ratio. For quantitative assessment, the near-wall profiles of TKE are presented in Fig. 11(e). From this figure, it can be seen that the near-wall TKE shows a good agreement between BR0 and BR5. For BR10, a slightly higher TKE is indicated. However, fore BR20, TKE sharply increases to higher values. Therefore, the near-wake flow with a higher blockage ratio is more turbulent. For the wake bi-stability behind the squareback Ahmed body, Burton *et al.* (2021) have proved that a high turbulence level of the background flow leads to highly frequent switches. Moreover, for the squareback Ahmed body, He *et al.* (2022) found that a higher TKE in the wake produced by a higher Reynolds number results in high-frequency wake switches, presenting a symmetric phenomenon. Therefore, the higher TKE observed with a higher blockage ratio can be a reason triggering frequently wake switches showing symmetry.

In addition, profiles of the near-wall mean streamwise velocity, $\overline{u}$, and mean negative pressure, $-\overline{C_p}$, in the X_1 plane are presented in Fig. 12. Distinctly higher $\overline{u}$ and $-\overline{C_p}$, as a result of the higher blockage influence, are observed with BR20. Therefore, the increase in the near-wake $\overline{u}$ and $-\overline{C_p}$ influences the wake structures. The literature showed that the bi-stable wake state of squareback Ahmed bodies is sensitive and easily broken by small perturbations of the wake (Cadot *et al.*, 2015; Evrard *et al.*, 2016; Barros *et al.*, 2017; Bonnavion and Cadot, 2018). In addition, for the notchback Ahmed body, He *et al.* (2021a) found that the bi-stable wake is sensitive to the suppression of the separation behind the rear slant. For this reason, one can speculate that the increase
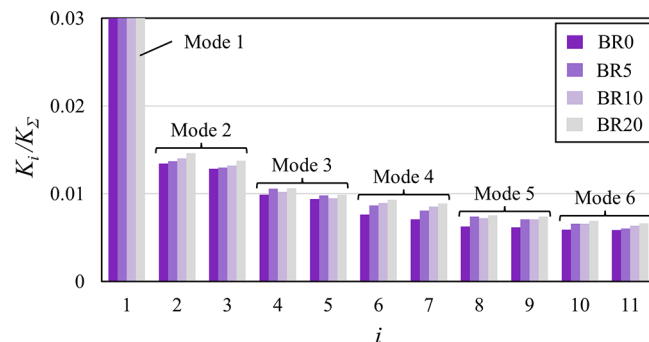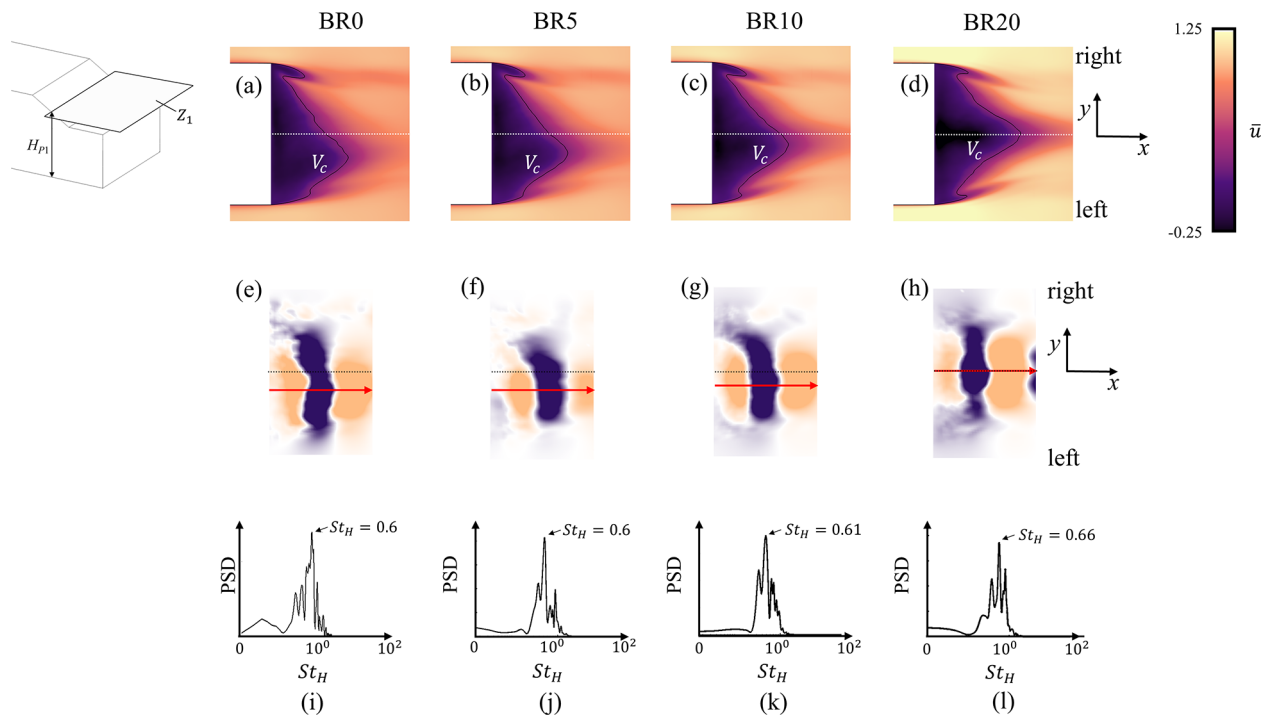
FIG. 9. Flow structures projected on the Z_1 plane, at $H_{P1} = 0.844H$ above the bottom body (located at half-height of the slant). (a)–(d) Distribution of the mean streamwise velocity, $\bar{u}$. (e)–(h) Mode 2 ($i = 2$) identified by POD. (i)–(l) The associated PSD of mode 2. Columns from left to right show the results of BR0, BR5, BR10, and BR20, respectively.
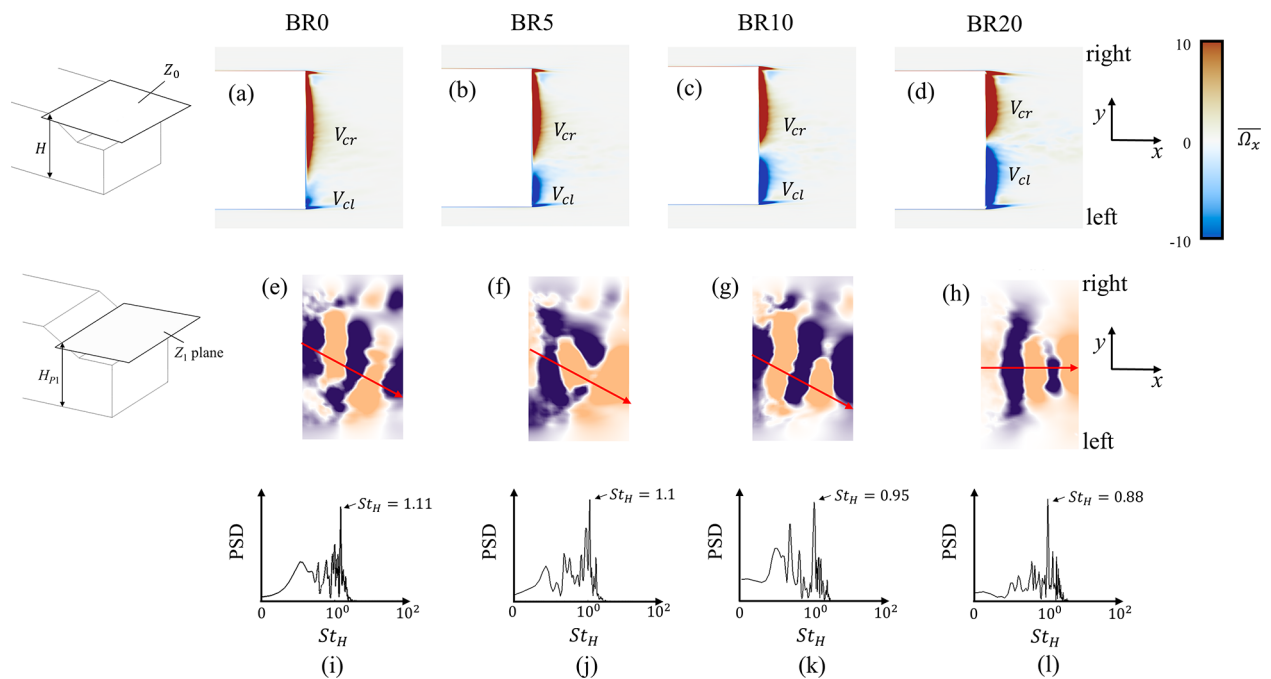

FIG. 10. (a)–(d) Distribution of the mean streamwise vorticity, $\overline{\Omega_x}$, projected on the Z_0 plane behind the upper slant. (e)–(h) Mode 4 identified by POD applying on the Z_1 plane. (i)–(l) The associated PSD of Mode 3 ($i = 4$). Columns from left to right show the results of BR0, BR5, BR10, and BR20, respectively.
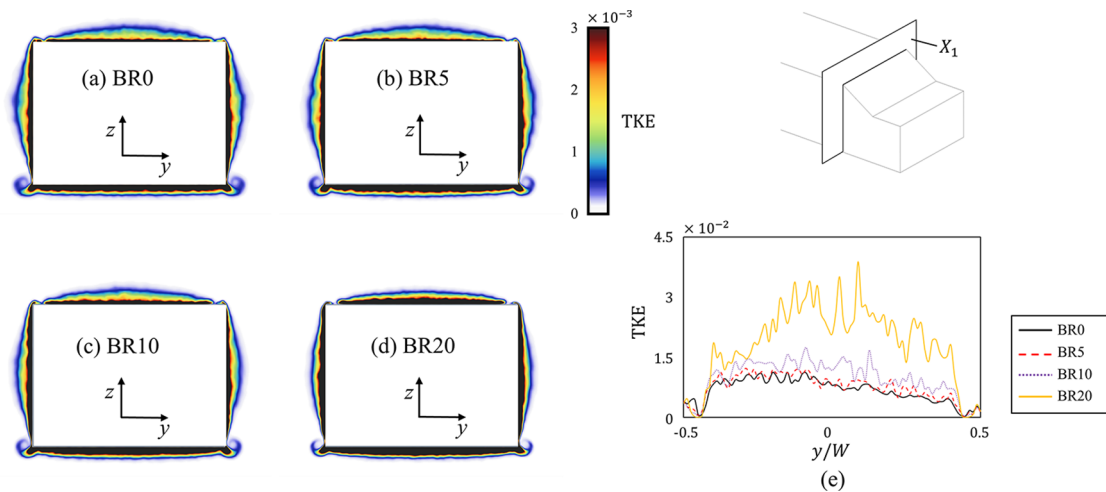
FIG. 11. Distribution of TKE in the cross section, X_1 plane, located at the linking edge between the roof and the slant. (a) BR0; (b) BR5; (c) BR10; (d) BR20. (e) Profiles of the near-wall TKE in the X_1 plane, obtained from the horizontal line at $0.01H$ above the roof's trailing edge.

in the near-wake velocity and negative pressure caused by a high blockage ratio disturb the state of the separation behind the slant, resulting in symmetrization of the wake structures.

C. Aerodynamic drags

The flow and pressure around the notchback Ahmed body have proved dependent on the blockage ratio. Thus, the aerodynamic drag associated with the surrounding flow is investigated for different blockages. The aerodynamic drag coefficient, C_d, can be divided into two parts, the viscous drag coefficient, C_{dv}, and the differential pressure drag coefficient, C_{dp}. The mean values of C_d, C_{dv}, and C_{dp} are plotted in Fig. 13. Considering the 95% confidence interval, the accuracy of the mean values is better than 1×10^{-4}. A general deduction from this figure is that lower $\overline{C_d}$, $\overline{C_{dv}}$, and $\overline{C_{dp}}$ are observed with the higher blockage ratio. Therefore, the aerodynamic drag with a certain blockage ratio is overestimated compared to BR0.

Reducing the blockage influence on the aerodynamic drag requires a correction. Therefore, several existing blockage corrections proposed in the literature are applied to the drag correction for the notchback Ahmed body. The equations for the drag correction are presented in Appendix C. The corrected aerodynamic

drag, $\overline{C_{dc}}$, is presented in Fig. 14. Compared to the $\overline{C_d}$ obtained from BR0 (shown in the black dotted line), the Maskell III equations proposed by Hackett and Cooper (2001) result in a good prediction of $\overline{C_{dc}}$, giving the deviation of 1.9%, 3.9%, and 4.3% for BR5, BR10, and BR20, respectively.

IV. CONCLUSIONS

The blockage influence on the bi-stable flow past a notchback Ahmed body is investigated using LES. Four different blockage ratios, 0%, 5%, 10%, and 20%, are considered. Although the wake asymmetry can be predicted under the blockage ratio within $0\% - 10\%$, the degree of wake asymmetry is found to decrease with the higher blockage ratio. The blockage ratio of 20% symmetrizes the bi-stable wake. The asymmetric state of the bi-stable flow under the low blockage and the wake symmetrization under blockage ratio of 20% is validated with the wind tunnel experiment.

The wake asymmetry is characterized by asymmetric separations and reattachments in the notchback region. The wake dynamics is identified by modal analysis applying POD. The wake structures and main frequencies show good agreement between the blockage ratio of 0% and 5%. The deflection of the flow structures behind the slant depends on the near-wall separations from the upper slant. The higher
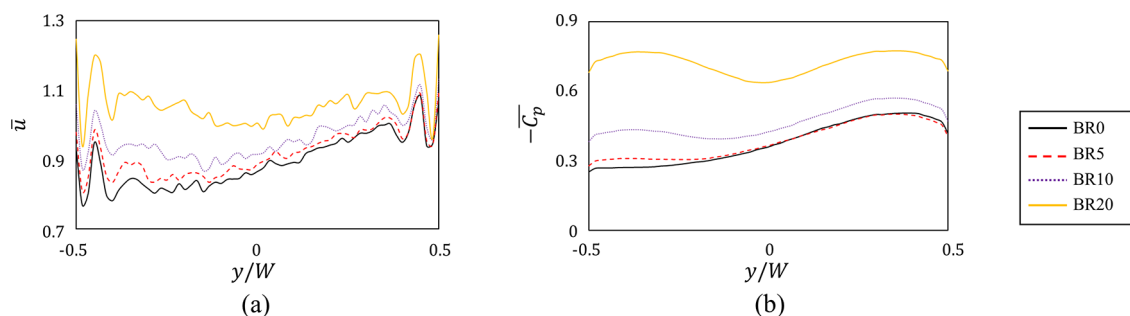

FIG. 12. Profiles of the near-wall (a) mean streamwise velocity, $\overline{u}$, and (b) mean negative pressure coefficient, $\overline{C_p}$, in the X_1 plane, obtained from the horizontal line at $0.01H$ above the roof's trailing edge.
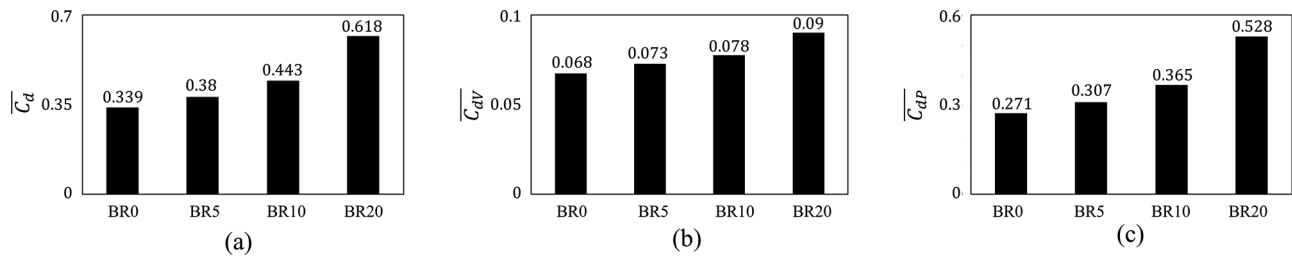
FIG. 13. Mean drag coefficients of the entire model change with blockage ratio. (a) The aerodynamic drag coefficient, $\overline{C_d}$. (b) The viscous drag coefficient, $\overline{C_{dv}}$. (c) The differential pressure drag coefficient, $\overline{C_{dp}}$.
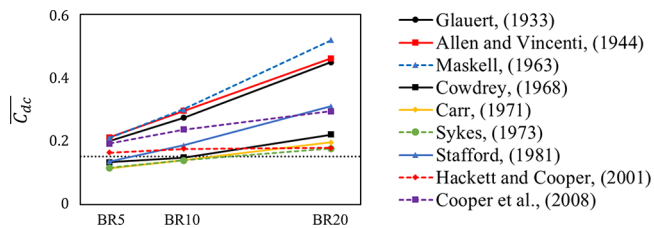

FIG. 14. Blockage corrections for the aerodynamic drag coefficients. The horizontal dotted line shown in black is the mean drag obtained in BR0 at $\overline{C_d} = 0.339$.

blockage ratio increases the turbulence kinetic energy, velocity, and negative pressure in the near-wake region. Therefore, the wake becomes more unstable to break the asymmetric state, resulting in the wake symmetrization under a 20% blockage ratio.

The aerodynamic drags, considering both the viscous drag and the differential pressure drag, are found to increase with the higher blockage ratio. Several existing equations for drag corrections proposed in the literature are applied for the notchback Ahmed body. The Maskell III equations proposed by Hackett and Cooper (2001) perform a good prediction for the drag correction.

The present work suggests the pronounced influence of the blockage ratio on the bi-stable wake behind the three-dimensional bluff body. The blockage ratio under 10% is enough to present the expected wake asymmetry. For accuracy of the asymmetry, the blockage ratio of less than 5% is recommended.

ACKNOWLEDGMENTS

AUTHOR DECLARATIONS
Conflict of Interest

The authors have no conflicts to disclose.

DATA AVAILABILITY

The data that support the findings of this study are available from the corresponding author upon reasonable request.

APPENDIX A: MESH RESOLUTION

Multi-block hexahedral conforming computational grids are made using the Pointwise grids generator. Meshes are mirrored, ensuring perfect mesh symmetry avoiding unexpected effects on the asymmetry of the flow. The computational cells are denser close to the surface of the model, and the spatial resolution around the forebody and in the wake region is finer than that around the middle body. The reason for this is that the flow separations around the rounded surface of the forebody and the wake structures require accurate prediction, but the flow around the middle body is undisturbed. The first layer of the computational cells throughout the model surface has a height of $3 \times 10^{-4} H$. The wall-normal growth factor near the model is 1.05, resulting in 70 layers of the grids attached to the boundary. In addition, to avoid the influence of the clearance between the body and the tunnel walls, the computational cells near the ground, roof, and two side walls are concentrated, and the height of the first layer near the

TABLE I. Details of the mesh.

| | Number of cells | Wall-normal resolution | Streamwise resolution | | Spanwise resolution |
			Fore and rear parts	Middle body	
BR0	3.3×10^7	$n^+ < 1$	$3 < \Delta_s^+ < 28$	$3 < \Delta_s^+ < 55$	$3 < \Delta_l^+ < 25$
BR5	4.2×10^7	$n^+ < 1$	$3 < \Delta_s^+ < 28$	$3 < \Delta_s^+ < 55$	$3 < \Delta_l^+ < 25$
BR10	3.9×10^7	$n^+ < 1$	$3 < \Delta_s^+ < 28$	$3 < \Delta_s^+ < 55$	$3 < \Delta_l^+ < 25$
BR20	3.6×10^7	$n^+ < 1$	$3 < \Delta_s^+ < 28$	$3 < \Delta_s^+ < 55$	$3 < \Delta_l^+ < 25$

tunnel walls is $4 \times 10^{-4}H$ with a growth factor of 1.2 in the wall-normal direction.

The numerical accuracy of the studied flow established by the grid-independence examination has been presented in the previously published work by the same author (He *et al.*, 2021c). In the present work, the mesh resolution is the same as the medium mesh used in He *et al.* (2021c). The number of cells and spatial resolutions is presented in Table I. Note that the fewer cells used for BR0 are attributed to the symmetry plane set at lateral walls and the roof of the flow domain. Thus, the velocity gradient in the wall-normal direction near the domain boundaries is almost 0, allowing stretched grids used.

APPENDIX B: VALIDATION

An experiment for the notchback Ahmed body is carried out in the closed-circuit wind tunnel at Chalmers University of Technology. Shown in Fig. 15(a) is the tested model with the height $H^* = 2H = 0.192$ m, giving the same shape as the model used in the simulation but twice as large. The forebody and the notchback configuration [the white parts of the body shown in Fig. 15(a)] are printed by a three-dimensional printer ensuring high precision of the frontal rounded surface and the effective backlight angle. The rest of the body is made of laser-cut planks. The model is mounted in a test section of $6.5H^* \times 9.4H^* \times 15.6H^*$ (height × width × length), giving a blockage ratio of 2.2%. The ground clearance of the underbody is $0.21H^*$ in agreement with the simulation. The body is supported by four vertical cylinders with a diameter of $0.1\,H^*$. The four supporters connect to the balance system under the ground, allowing the measurement of the aerodynamic forces. The inlet velocity of the wind tunnel varies within a range of 0–60 m/s.

The flow turbulence level is within 0.15% at a frequency range between 1 and 10 000 Hz. The Reynolds number based on H^* and the free-stream velocity is 5×10^4, the same as in the simulation. In addition, the model is equipped with pressure taps on the deck. The positions of the taps follow the pressure monitoring points for simulation shown in Fig. 6. The pressure data are obtained using a Scanivalve system (NetScanner TM model 9116). The pressure system has an accuracy of ±0.2 Pa for the used pressure range (±50 Pa) with a sampling frequency of 62.5 Hz.

The BR0 case cannot be investigated performed in the closed-circuit wind tunnel. Therefore, for the low blockage LES (BR0 and BR5), the validation considers the comparison to the experimental results under blockage ratio of 2.2% (BR2.2). For the high blockage case, the 20% blockage ratio following the BR20 simulation is achieved in the experiment by building a physical domain [Fig. 15(b)]. The time histories of the deck pressure gradient, $\partial C_{pd}/\partial y$, observed in the experiment, are presented in Figs. 15(c) and 15(d). For BR2.2, $\partial C_{pd}/\partial y$ undergoes periods with positive or negative values, showing bi-stability. The associated PDF suggests two mirrored asymmetric states, S_A and S_B. Each asymmetric state can last for tens of seconds until the stochastic shift to the opposite state. However, for BR20, $\partial C_{pd}/\partial y$ fluctuates around 0, and the associated PDF indicates the wake in the symmetric state, S_C.

To quantitate the degree of asymmetry between the experiment and LES, the mean value of $\partial C_{pd}/\partial y$ is used. For the experiment, $\overline{\partial C_{pd}/\partial y}$ is averaged from the pressure signals sampled during a period of 2 s. Particularly, for BR2.2, $\overline{\partial C_{pd}/\partial y}$ is sampled when the wake is in the S_B state with no switching processes. Furthermore, the mean drag coefficient, $\overline{C_d}$, is taken into account for the validation. The comparisons between the experiment and LES for the low and high blockage ratios are presented in
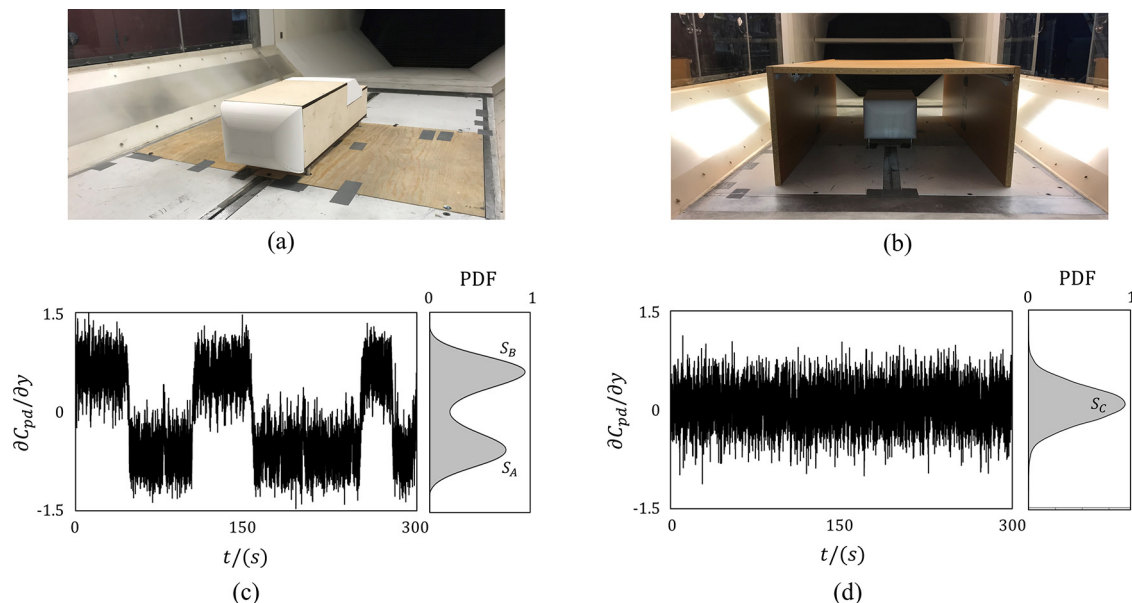

FIG. 15. The wind tunnel experiment. (a) The notchback Ahmed body mounted in the test section (BR2.2). (b) The body mounted in the physical domain (BR20). The time history of $\partial C_{pd}/\partial y$: (c) BR2.2; (d) BR20.

TABLE II. Comparisons of $\overline{\partial C_{pd}/\partial y}$ and $\overline{C_d}$ between the experiment and LES for the low blockage ratio.

	Experiment (BR2.2)	LES (BR0)	Deviation/ (%)	LES (BR5)	Deviation/ (%)
$\overline{\partial C_{pd}/\partial y}$	0.625	0.649	3.77	0.618	1.13
$\overline{C_d}$	0.364	0.339	7.11	0.38	4.56

TABLE III. Comparisons of $\overline{\partial C_{pd}/\partial y}$ and $\overline{C_d}$ between the experiment and LES for the high blockage ratio.

	Experiment (BR20)	LES (BR20)	Deviation/(%)
$\overline{\partial C_{pd}/\partial y}$	0.041	0.043	4.88
$\overline{C_d}$	0.631	0.618	2.08

Tables II and III. The deviation in each table considers the difference between the experimental and numerical results.

For the low blockage cases, the $\overline{\partial C_{pd}/\partial y}$ deviations are under 5%, showing good agreement. However, the $\overline{C_d}$ predicted by the BR0 simulation is somewhat smaller than that of the experiment. This is because the notchback geometry is suspended in the digital domain for LES, but the model in the wind tunnel experiment has to be supported. Therefore, the drag measured in the experiment is not only influenced by the blockage ratio given by the tunnel walls but also increased by the flow impinging on the underbody vertical cylinders. As a result, although the blockage ratios between the experiment and LES are not perfectly matched for the low blockage cases, results suggest a reasonably good agreement between them.

For BR20, the conformity between the experiment and LES is indicated in both $\overline{\partial C_{pd}/\partial y}$ and $\overline{C_d}$. Compared to the low blockage cases, the deviation of $\overline{C_d}$ is smaller under BR20. The reason is that the blockage ratio is perfectly matched between the experiment and LES for BR20. However, the higher $\overline{\partial C_{pd}/\partial y}$ deviation of BR20 compared to that of low blockage cases is because the values of $\partial C_{pd}/\partial y$ for the symmetric wake fluctuate around 0. Thus, the ratio of the difference to the mean values becomes larger due to the small $\overline{\partial C_{pd}/\partial y}$.

APPENDIX C: EQUATIONS FOR BLOCKAGE CORRECTIONS

In the present paper, several existing blockage corrections are applied to the notchback Ahmed body. Here, the equations abstracted from the literature are presented. Based on two-dimensional cylinders, Glauert (1933) provided a semi-empirical blockage correction

$$\frac{C_{dc}}{C_d} = \left[\frac{1 - G(S/C)}{1 + 0.822(S/C)^2}\right]^2, \tag{C1}$$

where C_{dc} is the corrected drag coefficient, S is the frontal projected area of the model, C is the cross-sectional area of the test section, and thus, S/C stands for the blockage ratio. G is an empirical factor, and Glauert (1933) suggested $G = 0.3$ for circular cylinders.

Considering the compressibility of the wake behind cylinders, Allen and Vincenti (1944) derived a theoretical model, expressed as

$$\frac{C_{dc}}{C_d} = 1 - \frac{\pi^2}{4}\left(\frac{S}{C}\right)^2 - \frac{C_d}{2}\left(\frac{S}{C}\right). \tag{C2}$$

Discussed by Maskell (1963), in the consideration of separated wake flows, the blockage correction for the drag can be derived based on a constant blockage factor, as

$$\frac{C_d}{C_{dc}} = 1 + \varepsilon C_d\left(\frac{S}{C}\right), \tag{C3}$$

where ε is the constant blockage factor. From the experimental data, Maskell suggested $\varepsilon = 0.96$ for bluff bodies with sharp edges.

Afterward, Cowdrey (1967) rederived the Maskell's equation and provided an improved blockage correction, which is not dependent on the measured drag, expressed as

$$\frac{C_d}{C_{dc}} = 1 + \mu\left(\frac{S}{C}\right), \tag{C4}$$

$$\mu = 1.85 + 1.35 e^{\left[-0.05\left(\frac{h}{w}\right)\right]}, \tag{C5}$$

where h and w are the height and width of the model, and thus, h/w stands for the aspect ratio of the model.

The continuity blockage correction formula, taking into account both mass and momentum conservation laws, was proposed by Carr (1971)

$$\frac{C_{dc}}{C_d} = \left(1 - \frac{S}{C}\right)^2. \tag{C6}$$

Sykes (1973) proposed a blockage correction with an empirical constant, expressed as

$$\frac{C_{dc}}{C_d} = 1 - m\frac{S}{C}, \tag{C7}$$

where m is the empirical constant. Sykes introduced $m = 1.9$ for rectangular bodies. After that, $m = 1.22$ was suggested by Stafford (1981) due to series of tests.

With additional solid and wake induced blockage terms, extensions to Maskell's original correction method were considered as Maskell III. This blockage correction was developed by Hackett and Cooper (2001) based on experimental data for bluff bodies. The formulas can be expressed as follows:

$$C_{dc} = \frac{C_d}{(1 + \varepsilon_T)^2}, \tag{C8}$$

$$\varepsilon_T = \varepsilon_S + \varepsilon_W, \tag{C9}$$

$$\varepsilon_S = 0.36\left(\frac{H^*}{W^*} + \frac{W^*}{H^*}\right)\left(\frac{V^*}{C^{*1.5}}\right), \tag{C10}$$

$$\varepsilon_W = \sqrt{1 + \theta\left(\frac{1}{1+\theta} - \frac{\Delta C_{dwi}}{C_d}\right)} - 1, \tag{C11}$$

$$\theta = \left(0.96 + 1.94 e^{-0.06 h/w}\right) C_d \frac{S^*}{C^*}, \qquad (C12)$$

where S^* and V^* are the duplex frontal projected area and the duplex volume of the model, respectively, and h/w is the aspect ratio of the model. W^*, H^*, and C^* are the duplex width, height and cross-sectional area of the test section, respectively. ΔC_{dwi} is the wake drag increment, which can be defined as

$$\Delta C_{dwi} = C_d \left(\frac{1}{1+\theta}\right) + \left(\frac{1}{2\theta}\right)\left(1 - \sqrt{1+4\theta}\right). \qquad (C13)$$

Subsequently, a further improved version, the Maskell III plus Thom equation, was proposed by Cooper *et al.* (2008). This correction considers the influence of both the wake and the solid blockage, expressed as

$$C_{dc} = \frac{C_d}{(1 + \varepsilon_S + \varepsilon'_w)^2} + \Delta C_{DM}, \qquad (C14)$$

$$\varepsilon'_w = \sqrt{1 + \frac{\theta C_d(S^*/C^*)}{1 + \theta C_d(S^*/C^*)} - \theta \Delta C_{DM}(S^*/C^*)} - 1, \qquad (C15)$$

where ε_S is given in Eq. (C10), θ is defined in Eq. (C12), and ΔC_{DM} is the Maskell III drag coefficient additive, defined as

$$\Delta C_{DM} = \frac{C_d}{1 + \theta C_d(S^*/C^*)} + \frac{1 - \sqrt{1 + 4\theta C_d(S^*/C^*)}}{2\theta(S^*/C^*)}. \qquad (C16)$$

REFERENCES

Ahmed, S. R., Ramm, G., and Faltin, G., "Some salient features of the time-averaged ground vehicle wake," in *SAE Transactions* (SAE International, 1984), pp. 473–503.

Aljure, D. E., Lehmkuhl, O., Rodríguez, I., and Oliva, A., "Flow and turbulent structures around simplified car models," Comput. Fluids **96**, 122–135 (2014).

Allen, H. J., and Vincenti, W. G., "Wall interference in a two-dimensional flow wind tunnel, with consideration for the effect of compressibility," NACA Technical Report No. 782, 1944.

Altinisik, A., Kutukceken, E., and Umur, H., "Experimental and numerical aerodynamic analysis of a passenger car: Influence of the blockage ratio on drag coefficient," J. Fluids Eng. **137**(8), 081104 (2015).

Barros, D., Borée, J., Cadot, O., Spohn, A., and Noack, B. R., "Forcing symmetry exchanges and flow reversals in turbulent wakes," J. Fluid Mech. **829**, R1 (2017).

Bonnavion, G., and Cadot, O., "Unstable wake dynamics of rectangular flat-backed bluff bodies with inclination and ground proximity," J. Fluid Mech. **854**, 196–232 (2018).

Buchheim, R., Unger, R., Carr, G. W., Cogotti, A., Garrone, A., Kuhn, A., and Nilsson, L. U., "Comparison tests between major European automotive wind tunnels," in *SAE Transactions* (SAE International, 1980), pp. 847–862.

Burton, D., Wang, S., Smith, D. T., Scott, H. N., Crouch, T. N., and Thompson, M. C., "The influence of background turbulence on Ahmed-body wake bistability," J. Fluid Mech. **926**, R1 (2021).

Cadot, O., Evrard, A., and Pastur, L., "Imperfect supercritical bifurcation in a three-dimensional turbulent wake," Phys. Rev. E **91**(6), 063005 (2015).

Carr, G. W., "Correlation of aerodynamic force measurements in MIRA and other automotive wind tunnels." SAE Technical Paper No. 820374, 1982.

Carr, G. W., "Influence of rear body shape on the aerodynamic characteristics of saloon cars," MIRA Report No. 1974/2, 1974.

Carr, G. W., "Wind tunnel blockage corrections for road vehicle," MIRA Report No. 1971/4, 1971.

Carr, G. W., and Stapleford, W. R., "Blockage effects in automotive wind-tunnel testing," SAE Technical Paper No. 860093, 1986.

Cogotti, A., "Car-wake imaging using a seven-hole probe," in *SAE Transactions* (SAE International, 1986), pp. 1071–1095.

Cogotti, A., Buchheim, R., Garrone, A., and Kuhn, A., "Comparison tests between some full-scale European automotive wind tunnelsÐPininfarina reference car," in *SAE Transactions* (SAE International, 1980), pp. 817–846.

Connor, C., Kharazi, A., Walter, J., and Martindale, B., "Comparison of wind tunnel configurations for testing closed-wheel race cars: A CFD study," SAE Technical Paper No. 2006-01-3620, 2006.

Cooper, K. R., Mokry, M., and Gleason, M., "The two-variable boundary-interference correction applied to automotive aerodynamic data," SAE Technical Paper No. 2008-01-1204, 2008.

Cowdrey, C. F., *The Application of Maskell's Theory of Wind-Tunnel Blockage to Very Large Solid Models* (National Physical Laboratory, 1967).

Dalla Longa, L., Evstafyeva, O., and Morgan, A. S., "Simulations of the bi-modal wake past three-dimensional blunt bluff bodies," J. Fluid Mech. **866**, 791–809 (2019).

Evrard, A., Cadot, O., Herbert, V., Ricot, D., Vigneron, R., and Délery, J., "Fluid force and symmetry breaking modes of a 3D bluff body with a base cavity," J. Fluids Struct. **61**, 99–114 (2016).

Evstafyeva, O., Morgans, A. S., and Dalla longa, L., "Simulation and feedback control of the Ahmed body flow exhibiting symmetry breaking behaviour," J. Fluid Mech. **817**, R2 (2017).

Glauert, H., "Wind tunnel interference on wings, bodies and airscrews," ARC Report No. ARC-R/M-1566 (Aeronautical Research Council, London, 1933).

Grandemange, M., Cadot, O., and Gohlke, M., "Reflectional symmetry breaking of the separated flow over three-dimensional bluff bodies," Phys. Rev. E **86**(3), 035302 (2012).

Grandemange, M., Gohlke, M., and Cadot, O., "Statistical axisymmetry of the turbulent sphere wake," Exp. Fluids **55**(11), 1838 (2014).

Grandemange, M., Gohlke, M., and Cadot, O., "Turbulent wake past a three-dimensional blunt body. Part 1. Global modes and bi-stability," J. Fluid Mech. **722**, 51–84 (2013).

Hackett, J. E., and Cooper, K. R., "Extensions to Maskell's theory for blockage effects on bluff bodies in a closed wind tunnel," Aeronaut. J. **105**(1050), 409–418 (2001).

He, K., Minelli, G., Su, X., Gao, G., and Krajnović, S., "Influence of the rounded rear edge on wake bi-stability of a notchback bluff body," Phys. Fluids **33**(11), 115107 (2021a).

He, K., Minelli, G., Wang, J. B., Dong, T. Y., Gao, G. J., and Krajnović, S., "Numerical investigation of the wake bi-stability behind a notchback Ahmed body," J. Fluid Mech. **926**, A36 (2021b).

He, K., Minelli, G., Wang, J. B., Gao, G. J., and Krajnović, S., "Assessment of LES, IDDES and RANS approaches for prediction of wakes behind notchback road vehicles," J. Wind Eng. Ind. Aerodyn. **217**, 104737 (2021c).

He, K., Minelli, G., Su, X., Gao, G., and Krajnović, S., "On state instability of the bi-stable flow past a notchback bluff body," J. Fluid Mech. **931**, R6 (2022).

Krajnović, S., and Davidson, L., "Flow around a simplified car, part 1: Large eddy simulation," J. Fluids Eng. Trans. ASME **127**(5), 907–918 (2005).

Lawson, N. J., Garry, K. P., and Faucompret, N., "An investigation of the flow characteristics in the Bootdeck region of a scale model notchback saloon vehicle," Proc. Inst. Mech. Eng. Part D: J. Automob. Eng. **221**(6), 739–754 (2007).

Lucas, J. M., Cadot, O., Herbert, V., Parpais, S., and Délery, J., "A numerical investigation of the asymmetric wake mode of a squareback Ahmed body-effect of a base cavity," J. Fluid Mech. **831**, 675–697 (2017).

Lumley, J. L., *Stochastic Tools in TurbulenceÐApplied Mathematics and Mechanics* (Academic Press, New York, 1970), Vol. 12.

Maskell, E. C., "A theory of the blockage effects on bluff bodies and stalled wings in a closed wind tunnel," ARC Report No. ARC-R/M-3400 (Aeronautical Research Council, London, 1963).

Mercker, E., "A blockage correction for automotive testing in a wind tunnel with closed test section," J. Wind Eng. Ind. Aerodyn. **22**(2–3), 149–167 (1986).

Nicoud, F., and Ducros, F., "Subgrid-scale stress modelling based on the square of the velocity gradient tensor," Flow Turbul. Combust. **62**(3), 183–200 (1999).

Östh, J., Noack, B. R., Krajnović, S., Barros, D., and Borée, J., "On the need for a nonlinear subscale turbulence term in POD models as exemplified for a high-

Reynolds-number flow over an Ahmed body," J. Fluid Mech. **747**, 518–544 (2014).

Pavia, G., Passmore, M. A., Varney, M., and Hodgson, G., "Salient three-dimensional features of the turbulent wake of a simplified square-back vehicle," J. Fluid Mech. **888**, A33 (2020).

Pavia, G., Passmore, M., and Sardu, C., "Evolution of the bi-stable wake of a square-back automotive shape," Exp. Fluids **59**(1), 20 (2018).

Pavia, G., Varney, M., Passmore, M., and Almond, M., "Three dimensional structure of the unsteady wake of an axisymmetric body," Phys. Fluids **31**(2), 025113 (2019).

Rigas, G., Oxlade, A. R., Morgans, A. S., and Morrison, J. F., "Low-dimensional dynamics of a turbulent axisymmetric wake," J. Fluid Mech. **755**, R5 (2014).

Sims-Williams, D., Marwood, D., and Sprot, A., "Links between notchback geometry, aerodynamic drag, flow asymmetry and unsteady wake structure," SAE Int. J. Passenger Cars. Mech. Syst. **4**(1), 156–165 (2011).

Sirovich, L., "Turbulence and the dynamics of coherent structures. I. Coherent structures," Q. Appl. Math. **45**(3), 561–571 (1987).

Stafford, L. G., "A streamline wind-tunnel working section for testing at high blockage ratios," J. Wind Eng. Ind. Aerodyn. **9**(1–2), 23–31 (1981).

Sykes, D. M., "Blockage corrections for large bluff bodies in wind tunnels," in *Advances in Road Vehicle Aerodynamics* (BHRA Fluid Engineering, 1973), pp. 311–321.

Takeda, K., and Kato, M., "Wind tunnel blockage effects on drag coefficient and wind-induced vibration," J. Wind Eng. Ind. Aerodyn. **42**(1–3), 897–908 (1992).

Wickern, G., "On the application of classical wind tunnel corrections for automotive bodies," in *SAE Transactions* (SAE International, 2001), pp. 708–734.

Yan, G., Xia, C., Zhou, H., Zhu, H., and Yang, Z., "Experimental investigation of the bi-stable behavior in the wake of a notchback MIRA model," SAE Technical Paper No. 2019-01-0663, 2019.

Yang, Z., Nastov, A., and Schenkel, M., "Further assessment of closed-wall wind tunnel blockage using CFD," in *SAE Transactions* (SAE International, 2005), pp. 939–949.